inorganics

MDPI

Article

Achieving Ultralong Room-Temperature Phosphorescence in Two-Dimensional Metal-Halide Perovskites by Tuning Alkyl Chain Length

Suqin Wang [1,†], Hui Zhu [1,†], Ming Sheng [1], Bo Shao [1], Yu He [1], Zhuang Liu [2,*], Min Li [3] and Guangtao Zhou [1,*]

[1] College of Engineering, Shandong Xiehe University, Jinan 250109, China
[2] School of Materials Science and Engineering, Shandong University, Jinan 250061, China
[3] School of Materials Science and Engineering, Nanjing University of Posts & Telecommunications, Nanjing 210023, China
* Correspondence: liu.zhuang@sdu.edu.cn (Z.L.); charlie@sdxiehe.edu.cn (G.Z.)
† These authors contributed equally to this work.

Abstract: Two-dimensional (2D) metal-halide perovskites with highly efficient room-temperature phosphorescence (RTP) are rare due to their complex structures and intricate intermolecular interactions. In this study, by varying the alkyl chain length in organic amines, we synthesized two 2D metal-halide perovskites, namely 4-POMACC and 4-POEACC, both of which exhibit significant RTP emission. Notably, 4-POMACC demonstrates a stronger green RTP emission with a significantly longer lifetime (254 ms) and a higher photoluminescence quantum yield (9.5%) compared to 4-POEACC. A thorough investigation of structural and optical properties reveals that shorter alkyl chains can enhance the optical performance due to reduced molecular vibrations and more effective exciton recombination. Computational calculations further show that the smaller energy gap between S_1 and T_n in 4-POMA facilitates intersystem crossing, thereby improving RTP performance. Based on their remarkable phosphorescence properties, we demonstrated their applications in information encryption. This work offers a novel design strategy that could inspire the development of next-generation RTP materials.

Keywords: room-temperature phosphorescence; two-dimensional; metal-halide perovskites; chain length; information encryption

check for updates

Academic Editors: Sake Wang, Nguyen Tuan Hung and Minglei Sun

Received: 31 January 2025
Revised: 28 March 2025
Accepted: 29 March 2025
Published: 1 April 2025

Citation: Wang, S.; Zhu, H.; Sheng, M.; Shao, B.; He, Y.; Liu, Z.; Li, M.; Zhou, G. Achieving Ultralong Room-Temperature Phosphorescence in Two-Dimensional Metal-Halide Perovskites by Tuning Alkyl Chain Length. *Inorganics* **2025**, *13*, 108. https://doi.org/10.3390/inorganics13040108

Copyright: © 2025 by the authors. Licensee MDPI, Basel, Switzerland. This article is an open access article distributed under the terms and conditions of the Creative Commons Attribution (CC BY) license (https://creativecommons.org/licenses/by/4.0/).

1. Introduction

Room-temperature phosphorescence (RTP) arising from the triplet excitons of organic molecules has garnered increased attention due to its substantial potential in a wide range of research fields, including display and lighting, secure encryption, chemical sensing, and information storage [1–5]. Among the various luminescent material systems, metal-halide perovskites offer numerous opportunities for the development of RTP materials, due to their wide-ranging structural and compositional versatility [6–10]. In particular, two dimensional (2D) metal-halide perovskites can be readily synthesized through a straightforward and low-temperature process, presenting an obvious advantage over organic materials [11–16]. Moreover, the rigid structure of 2D metal-halide perovskites helps reduce molecular vibrations, thereby suppressing non-radiative recombination and enhancing exciton emission [17–20]. Usually, the choice of metal cation largely determines the electronic structure of the 2D metal-halide perovskite and, hence, its emissive properties. In recent years, a number of Cd-based 2D metal-halide perovskites have been explored

mainly because of their interesting structural characteristics and the large band gap, which suggest that they may be good candidates for application as a luminescence matrix [21–24].

Organic spacer cations play a key role in the physicochemical properties of 2D metal-halide perovskites, that their size and chain length is crucial in altering the inorganic octahedra framework and determining the band gap [25–27]. In the past, extensive research has been conducted on the impact of the organic component chain length on the fluorescent properties of 2D metal-halide perovskite materials. Ye et al. investigated the photoluminescence properties of 2D metal-halide perovskite crystals synthesized with organic amines with different alkyl chain lengths [28]. The results prove that the chain length of organic amines can affect the arrangement of the inorganic layer octahedra, and the spectrum exhibits an obvious blue shift with extending alkyl chain. This study indicates that the alkyl chain length of the organic amines can be used to tune the structure and luminescent properties of 2D metal-halide perovskites. In addition, Liu et al. used two organic amines with different alkyl chain lengths as the organic components, and lead bromide as the inorganic component to synthesize two 2D metal-halide perovskites [29]. The photoluminescence from the as-prepared samples is attributed to the recombination of free excitons and self-trapped excitons. Moreover, the deeper exploration of the emission mechanisms demonstrates that by varying the alkyl chain length of the organic amines, the energy levels of the free and self-trapped excitons can be tuned accordingly. Furthermore, Palstra et al. found that the different chain lengths of alkyl in the organic amines influenced the optical bandgap of materials by varying the framework of the inorganic layer [30]. For example, short-chain organic amines resulted in corner-shared octahedra, while long-chain amines lead to both corner-sharing and face-sharing octahedra. Therefore, adjusting the alkyl chain length of organic amines is a powerful tool for tuning the optical band gap and luminescent properties of 2D metal-halide perovskites. However, investigations on the modulation of RTP in 2D metal-halide perovskites using organic amines with varying alkyl chain lengths are still relatively scarce.

In this work, two organic amines with different alkyl chain lengths, namely 4-phenoxybenzylamine (4-POMA) and 4-phenoxyphenethylamine (4-POEA), are selected as the organic components, with $CdCl_2$ as the inorganic component. Using a simple synthesis method, two 2D metal-halide perovskite materials (4-POMACC and 4-POEACC) with distinct RTP properties are synthesized. Photophysical characterizations reveal that both materials exhibit dual-peak emissions, while there are notable differences in their RTP lifetimes. Specifically, 4-POMACC has lifetimes of 254 ms, whereas 4-POEACC has a lifetime of only 68 ms. Additionally, the quantum efficiencies of the two materials are 9.50% and 8.06%, respectively. The interlayer spacing calculations are employed to further investigate the origins of their RTP characteristics. Based on their RTP properties, the materials are explored for anti-counterfeiting applications. The research findings of this work demonstrate that the alkyl chain length of organic amines has a significant impact on the RTP properties of 2D metal-halide perovskites.

2. Results and Discussion

By performing powder X-ray diffraction (PXRD) analysis on 4-POMACC and 4-POEACC, the layered structure characteristic of 2D metal-halide perovskites can be confirmed. As shown in Figure 1, PXRD patterns indicate that the synthesized materials exhibit structural features similar to those reported for 2D metal-halide perovskites, that both 4-POMACC and 4-POEACC display strong periodic diffraction peaks corresponding to the (00l) crystal planes, with no significant diffraction peaks observed from other crystal planes. This result suggests that both materials preferentially grow along the c-axis, favoring the formation of a layered structure with alternating inorganic and organic layers [31,32]. The

diffraction peaks of the (00l) planes are sharp and intense, indicating that both materials possess good crystallinity. In Figure 1a, when comparing the PXRD pattern of 4-POMACC with its corresponding organic amine salt (4-POMACl) and inorganic component ($CdCl_2$), it is observed that the diffraction peaks of 4-POMACC are slightly shifted relative to those of 4-POMACl and do not correspond to the peak positions of $CdCl_2$. This result confirms the successful synthesis of a well-crystallized 2D metal-halide perovskite material. Similarly, in Figure 1b, 4-POEACC exhibits a clear layered structural feature with improved crystallinity and orientation compared to 4-POEACl, and it does not display the characteristic diffraction peaks of $CdCl_2$.

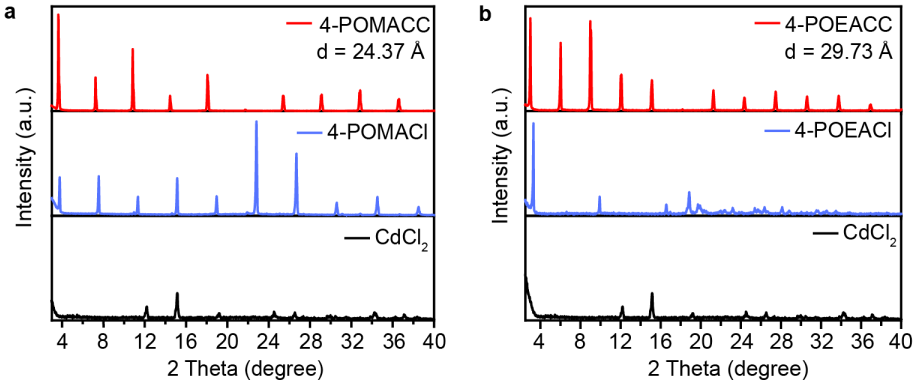


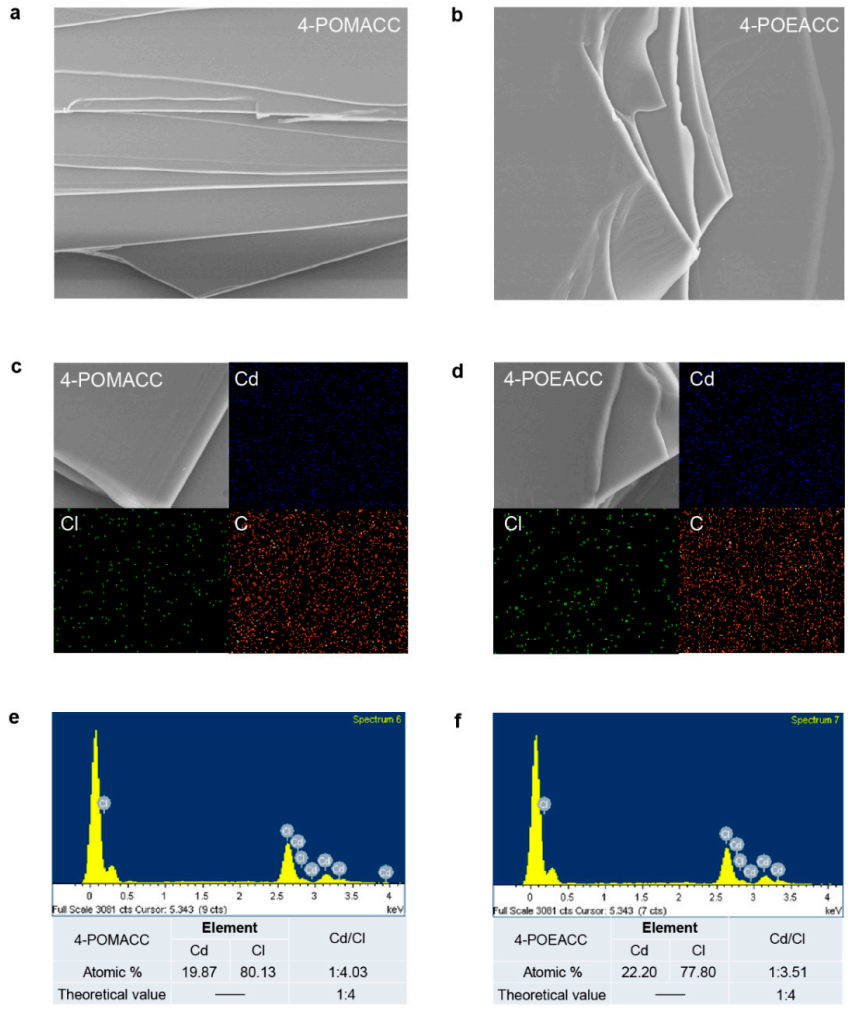
Figure 1. PXRD patterns of (**a**) 4-POMACC and (**b**) 4-POEACC, as well as their corresponding organic amine salts (4-POMACl and 4-POEACl) and inorganic salts ($CdCl_2$).

Two-dimensional metal-halide perovskites possess a layered structure, and one of their key characteristics is described by interlayer spacing (d), which refers to the distance between adjacent inorganic layers within the material's structure. This spacing can be calculated using PXRD data and Bragg's equation ($2d\sin\theta = n\lambda$, where θ denotes the diffraction angle, λ stands for the X-ray wavelength, and n refers to the diffraction order). The calculated results in this work are 24.37 Å for 4-POMACC and 29.73 Å for 4-POEACC. This difference arises because 4-POEACl contains an additional methyl group compared to 4-POMACl. Therefore, the larger organic molecule leads to greater interlayer spacing and looser packing of organic molecules. As a result, the molecular vibration becomes stronger, which is detrimental to luminescence [33].

The vibrational peak positions obtained from Fourier transform infrared (FTIR) spectroscopy can be used to identify specific functional groups and chemical bonds within a material, allowing for further inference about the internal structure and vibrational modes of organic components. As shown in Figure S3, all four species (4-POMACl, 4-POEACl, 4-POMACC, and 4-POEACC) exhibit a hydroxyl (-OH) vibrational peak between 3400 and 3500 cm^{-1}, likely due to water absorption from the air. Comparing the FTIR patterns of 4-POMACC and 4-POEACC, one can find that both of them show the presence of amino ($-NH_2$) vibrational peaks, corresponding to the vibrational modes of the functional groups in the reactants. In Figure S3a, the N-H vibrational peak of 4-POMACC (3176 cm^{-1}) is shifted to a higher frequency compared to that in 4-POMACl (2995 cm^{-1}), which is because the amino group ($-NH_3^+$) in 4-POMACC forms hydrogen bonds (N-H···Cl) with the inorganic layer. The formation of hydrogen bonds generally reduces the vibrational frequency (or peak value) of N-H. In contrast, in 4-POMACl, the $-NH_3^+$ group forms ionic bonds with free Cl^- ions, resulting in a stronger ionic interaction compared to the hydrogen bonding in 4-POMACC. This difference in bond types causes a noticeable shift in the N-H vibrational peaks. These observations further confirm that in 4-POMACC, the organic and inorganic layers are connected through N-H···Cl hydrogen bonds, which facilitate the formation of

the 2D perovskite structure. Similarly, Figure S3b demonstrates that 4-POEACC exhibits the same structural characteristic, indicating the presence of N-H···Cl hydrogen bonds as well.

Scanning electron microscopy (SEM) is used to observe the microstructure of materials, providing insight into their morphological characteristics. As shown in Figure 2a,b, both 4-POMACC and 4-POEACC exhibit a layered structure formed by the stacking of sheet-like growths, indicating that the synthesized materials possess the layered characteristic [34]. Notably, the sheets of 4-POEACC appear to be thicker than those of 4-POMACC, likely due to the increased carbon chain length in the organic component, which may lead to poorer sheet formation and a tendency for agglomeration. Elemental mapping, as shown in Figure 2c,d, reveals that the elements Cd, Cl, and C are evenly distributed throughout in both 2D metal-halide perovskites. To further confirm the 2D structure of the synthesized materials, energy-dispersive X-ray spectroscopy (EDS) analysis was performed. As seen in Figure 2e,f, the actual molar ratios of Cd to Cl are 1:4.03 and 1:3.51, respectively, which are close to the theoretical molar ratio of 1:4 for 2D metal-halide perovskites. This result confirms that both materials exhibit the characteristic features of 2D metal-halide perovskites, and their chemical formulas are $(4\text{-POMA})_2CdCl_4$ and $(4\text{-POEA})_2CdCl_4$, respectively.



4-POMACC	Element		Cd/Cl
	Cd	Cl	
Atomic %	19.87	80.13	1:4.03
Theoretical value	——		1:4

4-POEACC	Element		Cd/Cl
	Cd	Cl	
Atomic %	22.20	77.80	1:3.51
Theoretical value	——		1:4

Figure 2. SEM images of (**a**) 4-POMACC and (**b**) 4-POEACC. Element mapping results of (**c**) 4-POMACC and (**d**) 4-POEACC. Energy-dispersive X-ray spectroscopy results of (**e**) 4-POMACC and (**f**) 4-POEACC. The picture size in (**a**,**b**) and (**c**,**d**) are 10 × 10 um and 2 × 2 um, respectively.

Thermal stability is a key property of metal-halide perovskites, in that the greater the thermal stability, the more capable the metal-halide perovskite is of maintaining long-term performance in high-temperature environments [35]. From the thermogravimetric analysis (TGA) shown in Figure S4a,c, it is evident that the initial thermal decomposition temperature of 4-POMACC is 263 °C, which is 41 °C higher than that of 4-POMACl. This improvement in thermal stability can be attributed to the formation of the 2D metal-halide structure in 4-POMACC compared to 4-POMACl, which increases the rigidity of the materials. The derivative thermogravimetry (DTG) curve of 4-POMACl reveals two distinct weight loss peaks, which are due to the two-step decomposition of the organic components. The absence of a clear weight loss plateau suggests that these two decomposition processes overlap. In contrast, the DTG curve of 4-POMACC shows an additional weight loss peak, which is attributed to the decomposition of the inorganic components. This further confirms that 4-POMACC is a 2D metal-halide perovskite material, formed by the self-assembly of both organic and inorganic components. In detail, 4-POMACC exhibits a weight loss of 5.96% in the temperature range of 263 °C to 297 °C, and this loss reaches 44.43% at 589 °C. It is speculated that the lost groups transform from HCl and NH_2 to $C_{13}H_{11}O$. Beyond 589 °C, reactions involving the inorganic components occur, including the volatilization and decomposition of $CdCl_2$, followed by the oxidation of elemental cadmium in the presence of air. For 4-POMACl, nearly all organic components decompose before 603 °C, which is close to the decomposition temperature (589 °C) of organic components in 4-POMACC. Similarly, 4-POEACC decomposes at 253 °C, a lower temperature compared to 4-POMACC, indicating that 4-POMACC has good thermal stability. Furthermore, as seen in Figure S4b,d, the decomposition temperature of 4-POEACC is 38 °C higher than that of 4-POEACl, and like 4-POMACC, it undergoes decomposition of both organic and inorganic components. This suggests that 4-POEACC is also a 2D metal-halide perovskite material formed through the self-assembly of organic and inorganic constituents.

We further study the optical properties of these two 2D metal-halide perovskite materials. Figure 3a,b display the solid-state UV diffuse reflectance spectra of 4-POMACC and 4-POEACC. In the 200 nm to 400 nm range, 4-POMACC exhibits strong absorption, while in the visible light region from 400 nm to 800 nm, it shows weaker absorption, with the most intense absorption peak at 275 nm. Similarly, 4-POEACC shows absorption in the 200 nm to 400 nm range, comparable to that of 4-POMACC, but its absorption in the visible region is limited to the 400 nm to 600 nm range, with the strongest absorption peak at 280 nm. When comparing the absorption peak positions of the two materials, it is observed that the peak position of 4-POEACC is red-shifted relative to that of 4-POMACC. This red shift can be attributed to the longer alkyl chain of the organic amine in 4-POEACC, which enhances the intermolecular interactions among the organic amine chains [36]. As a result, the coordination field of the halide ion is weakened, leading to a reduction in the splitting energy of the inorganic cadmium ions, thereby causing the absorption peak to shift to a longer wavelength. In addition, Tauc plots were further conducted to determine the optical band gaps of these two materials. As shown in Figure 3c,d, their indirect optical band gaps are 4.25 eV for 4-POMACC and 4.19 eV for 4-POEACC, respectively. The close similarity in the indirect optical band gaps of these two materials can be attributed to their analogous coordination environments and symmetry, especially evident in the inorganic layers, where both materials are composed of $CdCl_2$. Additionally, the organic components of the two materials are nearly identical, differing only by a single $–CH_2$ group.

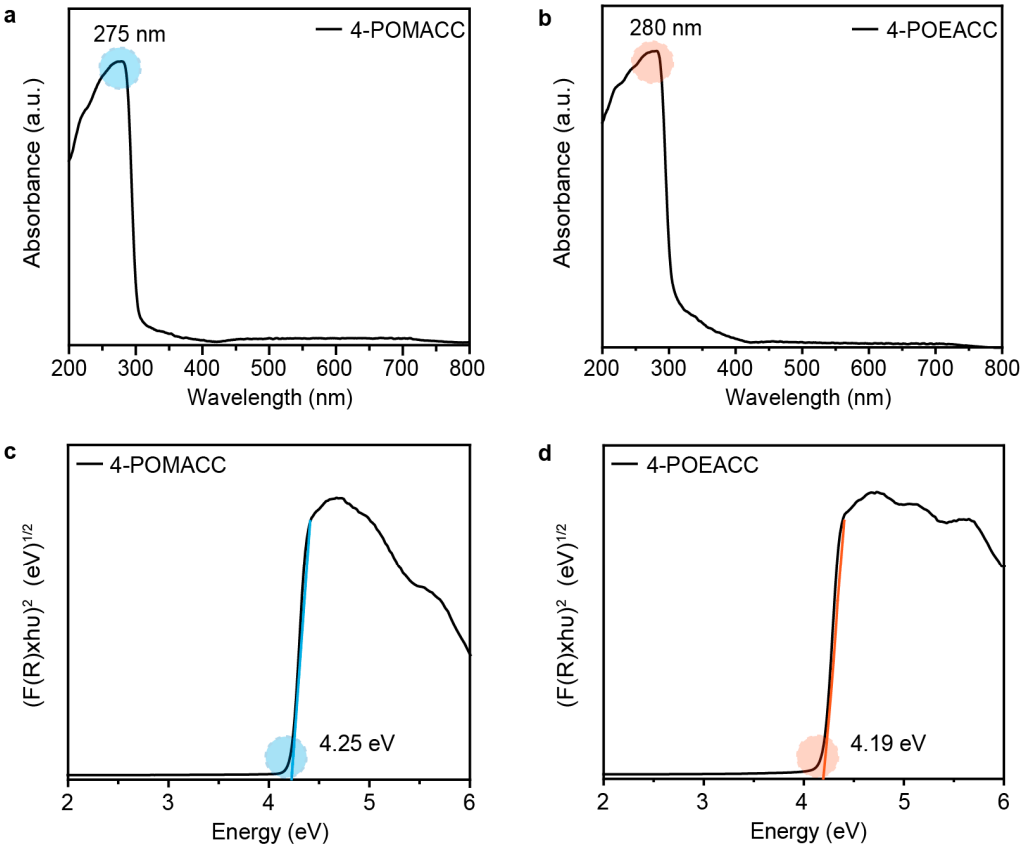


Figure 3. Diffuse reflectance spectra of (**a**) 4-POMACC and (**b**) 4-POEACC. Tauc plots of (**c**) 4-POMACC and (**d**) 4-POEACC according to their absorption spectra.

To investigate the effect of different organic amines on the luminescent properties of the materials, we then conducted photophysical characterizations. Phosphorescence spectra were obtained using an Edinburgh FLS980 fluorescence spectrophotometer with a 10 ms delay time after excitation using a microsecond flash lamp. Figure 4a displays the steady-state photoluminescence spectrum (black curve) and phosphorescence spectrum (cyan curve) of 4-POMACC. The steady-state photoluminescence spectrum was measured under excitation at a wavelength of 270 nm, while the phosphorescence spectrum was recorded under excitation at 286 nm. The steady-state spectrum of 4-POMACC shows a sharp emission peak at 305 nm, along with a weaker emission band in the 450–700 nm range, which may be attributed to the phosphorescence. Figure 4b shows the steady-state photoluminescence spectrum (brown curve) and phosphorescence spectrum (green curve) of 4-POEACC. The version 4-POEACC exhibits a sharp emission peak at 310 nm but lacks the long-wavelength emission observed in 4-POMACC. After turning off the UV lamp, 4-POMACC exhibits a green RTP. The phosphorescence spectrum reveals a dual-peak emission at 495 nm and 595 nm, with the intensity of the first peak being stronger. Although 4-POEACC's RTP is barely visible to the naked eye, it also displays dual-peak emissions at 505 nm and 615 nm, but with an intensity pattern opposite to that of 4-POMACC. Comparing the emission peaks of 4-POMACC and 4-POEACC, it is evident that both the fluorescence and phosphorescence emissions exhibit red shifts as the alkyl chain length of the organic amine increases, consistent with the red shift observed in their respective absorption spectra.

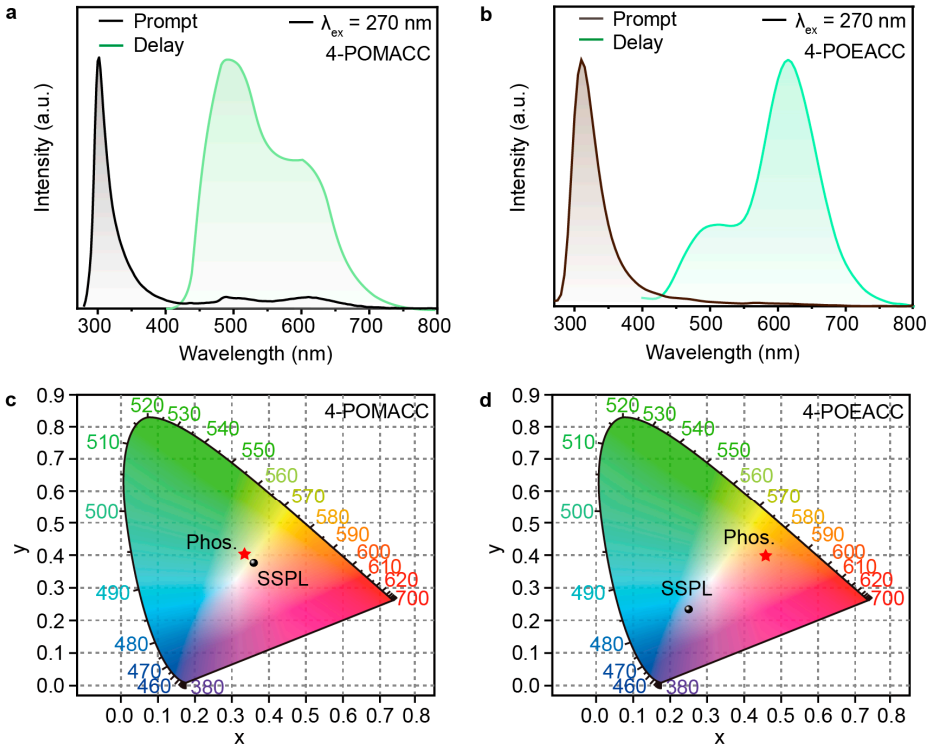


Figure 4. Steady-state photoluminescence and phosphorescence spectra of (**a**) 4-POMACC and (**b**) 4-POEACC excited at 270 nm. CIE coordinate diagrams of (**c**) 4-POMACC and (**d**) 4-POEACC.

To gain a clearer understanding of the colors exhibited by the materials, we used the Commission Internationale de l'Eclairage (CIE) standard color measurement system to process and calculate the steady-state and phosphorescence spectra data. As shown in Figure 4c,d, the fluorescence color coordinates of 4-POMACC are (0.36, 0.38), corresponding to a hue that leans toward the orange–yellow region. The phosphorescence color coordinates are (0.33, 0.41), indicating a hue that leans toward the yellow–green region, with both fluorescence and phosphorescence occupying similar color spaces. In contrast, 4-POEACC exhibits fluorescence color coordinates of (0.25, 0.23), placing its hue in the ultraviolet region. The phosphorescence color coordinates are (0.46, 0.40), indicating a shift toward the orange–red region. The significant difference between the fluorescence and phosphorescence color regions for 4-POEACC contrasts sharply with the close color proximity observed in 4-POMACC.

Time-resolved spectroscopy was then employed to measure the lifetimes of these two materials, providing a metric for comparing the RTP characteristics of the two samples. Figure 5a,c display the fluorescence and phosphorescence decay curves of 4-POMACC. As illustrated, the fluorescence emission peak at 305 nm exhibits a lifetime of only 1.98 ns, characteristic of singlet exciton radiative recombination. In contrast, the phosphorescence emissions at 495 nm and 595 nm have lifetimes of 322 ms and 240 ms, respectively, indicative of triplet exciton radiative recombination. Similarly, Figure 5b,d show the fluorescence and phosphorescence decay curves of 4-POEACC. The fluorescence emission peak at 310 nm has a lifetime of 1.12 ns, also representative of singlet exciton emission. However, the phosphorescence emissions at 505 nm and 615 nm exhibit much shorter lifetimes of 68 ms and 33 ms, respectively, reflecting triplet exciton emission. As a result, for both fluorescence and phosphorescence, 4-POMACC demonstrates significantly longer lifetimes than 4-POEACC.

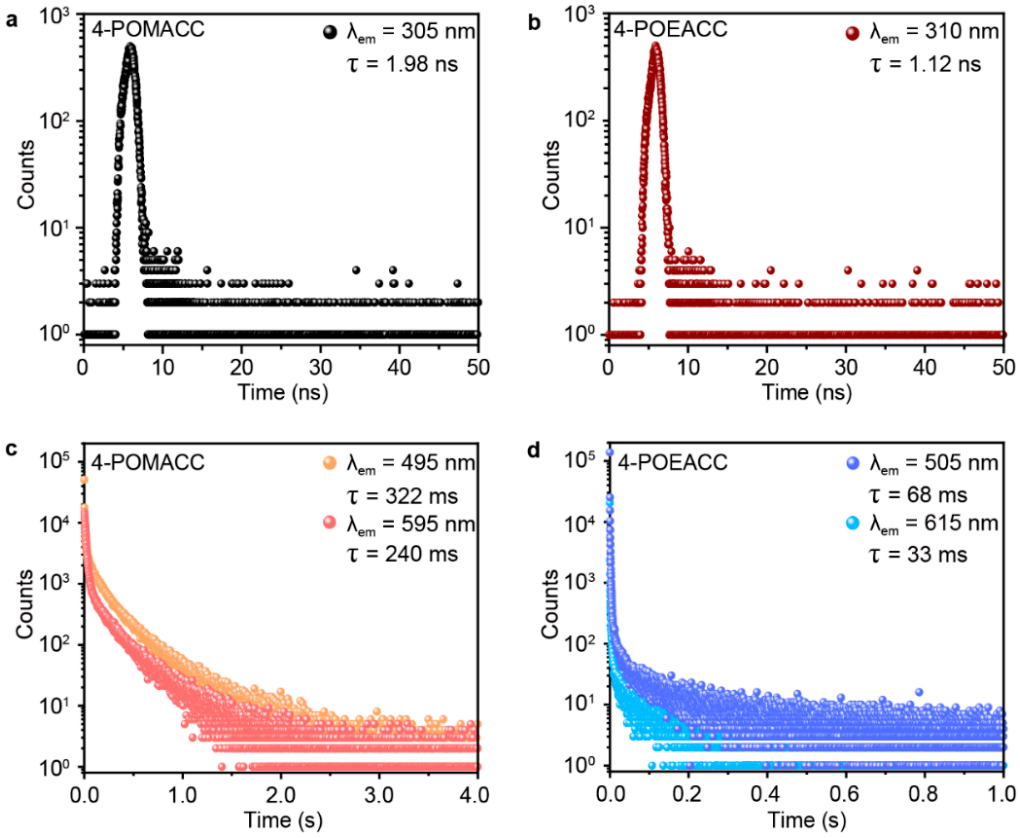


Figure 5. Time-resolved spectroscopy of (**a**,**b**) fluorescence and (**c**,**d**) phosphorescence for 4-POMACC (**left**) and 4-POEACC (**right**).

To provide a more comprehensive comparison of phosphorescence performance across the entire spectral range, time-resolved emission spectroscopy (TRES) was conducted. Figure S5a,b present the TRES patterns for 4-POMACC and 4-POEACC under 286 nm and 284 nm excitation, respectively. The results reveal that both 4-POMACC and 4-POEACC exhibit a gradual decrease in emission intensity over time. Notably, 4-POMACC maintains an emission intensity at level 3 even after a delay of 2 s. In contrast, 4-POEACC reaches the same intensity level only after a delay of 0.5 s. This comparison demonstrates that 4-POMACC has a longer phosphorescence lifetime across the entire spectral range.

The photoluminescence quantum yield (PLQY) is defined as the ratio of the number of emitted photons to the number of absorbed photons, providing a direct measure of the material's luminescence intensity [37]. As illustrated in Figure S6a,b, the PLQY of 4-POMACC increased from 6.00% for 4-POMACl to 9.50%. This enhancement is attributed to the rigid structure of 4-POMACC. The PLQY of 4-POEACC improved compared to 4-POEACl, as shown in Figure S6c,d. It is speculated that the introduced inorganic halide framework can effectively suppress the vibrations of organic molecules and reduce non-radiative recombination [38].

To elucidate the origin of the luminescence in these two 2D metal-halide perovskites, we performed spectral comparisons between the materials and their corresponding organic amine salts. Figure 6a,b show the fluorescence and phosphorescence spectra for 4-POMACC and 4-POMACl. It is observed that the fluorescence emission peak of 4-POMACC is centered around 305 nm, which is similar to the fluorescence emission peak of 4-POMACl. Additionally, 4-POMACC exhibits dual peaks of phosphorescence around 495 nm and 595 nm, whereas 4-POMACl displays a single peak of phosphorescence centered at 495 nm. This indicates that the fluorescence at 305 nm and the phosphorescence at 495 nm in 4-POMACC originate from the organic amine salt 4-POMACl. Based on previous

reports on perovskite defect luminescence, the phosphorescence emission peak at 595 nm is likely due to defect emissions caused by distortions in the inorganic lattice [39]. Similarly, as shown in Figure 6c,d, the fluorescence emission at 310 nm in 4-POEACC is attributed to the organic amine salt 4-POEACl, while the phosphorescence emissions at 505 nm and 615 nm are sourced from the organic amine salt 4-POEACl, with the 615 nm emission also being ascribed to defect emission due to lattice distortions in the inorganic layer. Note that, the fluorescence spectra of the two compounds in this work appear similar because their emission originates from A-site organic parts, but not from the bandgap emission, which is similar to previously reported Cd-based organic–inorganic hybrid halide perovskites, such as ABA_2CdCl_4 and $(F_2CHCH_2NH_3)_2CdBr_4$ [40,41].

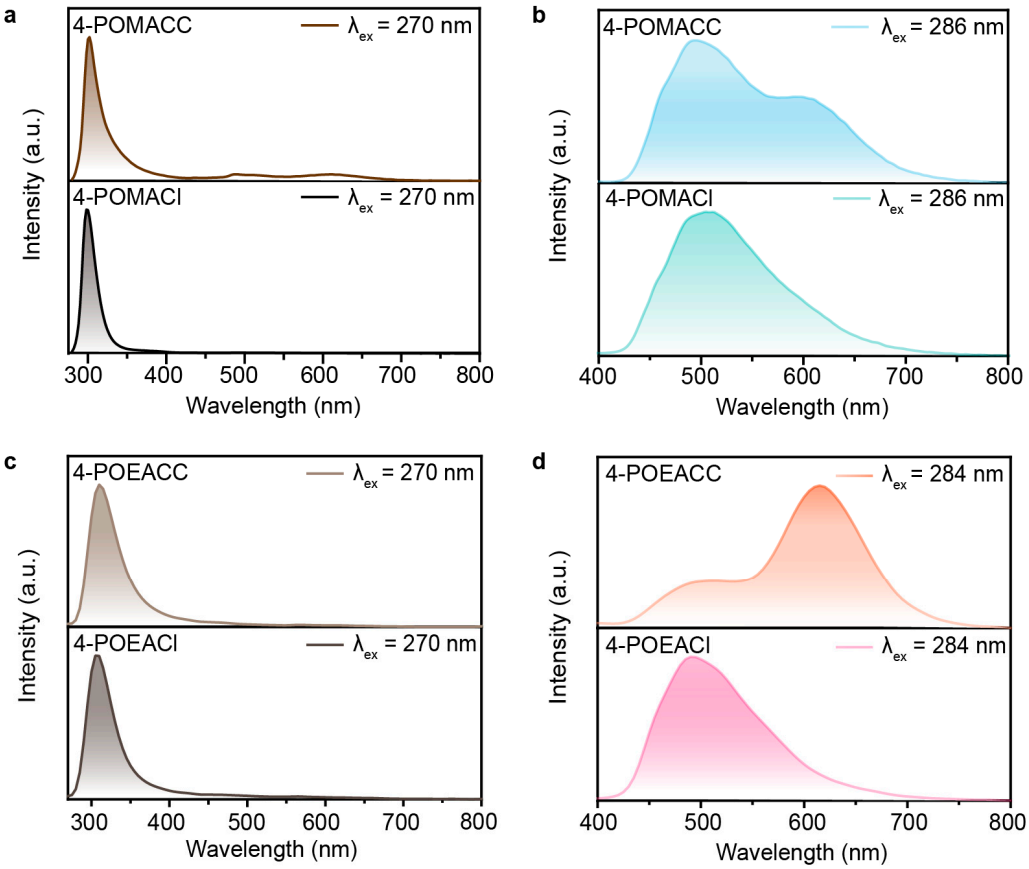


Figure 6. (**a**) Steady-state spectra of 4-POMACC and 4-POMACl. (**b**) Phosphorescence spectra of 4-POMACC and 4-POMACl. (**c**) Steady-state spectra of 4-POEACC and 4-POEACl. (**d**) Phosphorescence spectra of 4-POEACC and 4-POEAC.

To further verify that the 595 nm emission peak of 4-POMACC and the 615 nm emission peak of 4-POEACC are due to defect emission from lattice distortions in the inorganic layers, we conducted spectral tests under varying excitation powers. The relationship between emission intensity and excitation power was analyzed using a power law equation ($y = y_0 + x^n$), where n is a parameter that indicates the type of recombination mechanism [42]. When n is less than 1, it typically corresponds to defect state recombination; when n ranges from 1 to 2, it indicates free exciton recombination; and when n is equal to 2, it is associated with band-to-band recombination. From Figure S7, the fitting results show that the value of n for 4-POMACC is 0.84 and for 4-POEACC is 0.92. Since both values of n are less than 1, this suggests that the 595 nm emission in 4-POMACC and the 615 nm emission in 4-POEACC can be attributed to defect state luminescence.

To investigate the effects of excitation intensity and duration on the optical properties of materials, we conducted corresponding kinetic tests. As shown in Figure 7a,b, the emission intensity of both 4-POMACC and 4-POEACC increases with rising radiation flux. At 10% of the radiation flux (with an excitation intensity of 30 μW/cm^2), both materials can be effectively excited. Additionally, as shown in Figure 7c,d, both 4-POMACC and 4-POEACC exhibit stable luminescence during the 10 s excitation period; however, 4-POMACC shows greater stability compared to 4-POEACC during excitation. After 10 s of excitation, 4-POMACC displays a distinct exponential decay, whereas 4-POEACC shows a less pronounced exponential decay. Furthermore, as the excitation duration is extended, the emission intensity of both 4-POMACC and 4-POEACC also increases. This outcome suggests that the optical properties of these materials are influenced by both radiation flux and excitation duration.

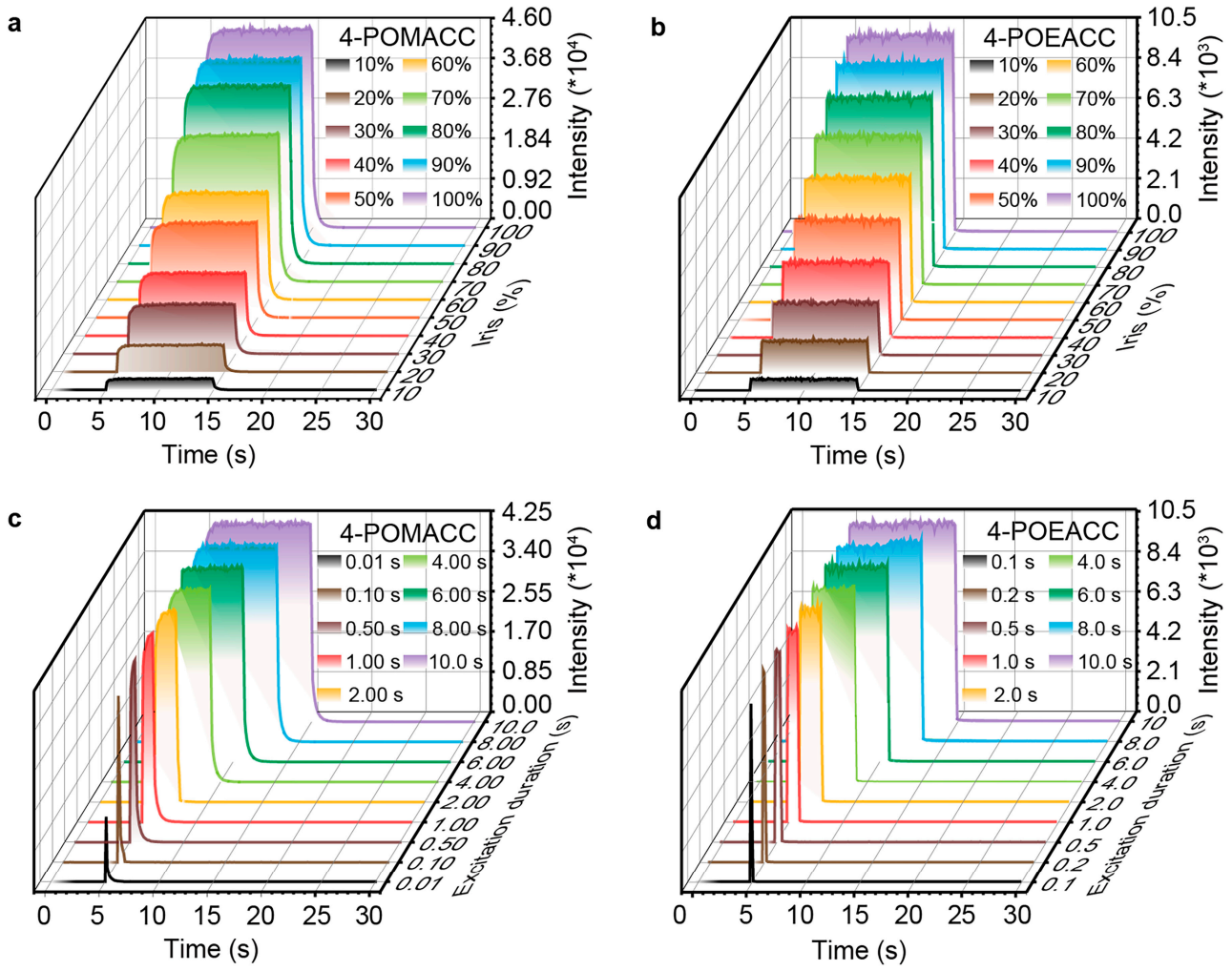


Figure 7. Emission intensity of 4-POMACC as functions of (**a**) radiation intensity and (**c**) excitation duration (excitation at 286 nm, emission at 495 nm). Emission intensity of 4-POEACC as functions of (**b**) radiation intensity and (**d**) excitation duration (excitation at 284 nm, emission at 505 nm).

To quantitatively analyze the impact of radiation flux and excitation duration on the optical properties of the two materials, we further compared their fluorescence and phosphorescence intensities under identical radiation flux and excitation durations. Figure S8a,b display their fluorescence and phosphorescence intensities as a function of varying radiation fluxes. At the same radiation flux, 4-POMACC exhibits significantly higher fluorescence and phosphorescence intensities than 4-POEACC. Furthermore, for the same

range of radiation flux variations, 4-POMACC shows a greater increase in intensity compared to 4-POEACC. These results indicate that the fluorescence and phosphorescence properties of 4-POMACC surpass those of 4-POEACC. Similarly, Figure S8c,d present the fluorescence and phosphorescence intensities of both materials under different excitation durations. However, as the excitation duration is extended, the increase in fluorescence and phosphorescence intensities for 4-POMACC is less pronounced, whereas the intensities for 4-POEACC remain relatively unchanged. This phenomenon, known as light activation, reflects an enhancement in luminescence intensity with prolonged excitation duration. The results suggest that 4-POMACC exhibits a notable light activation effect, while 4-POEACC shows minimal or no light activation.

To investigate the effect of different excitation wavelengths on the luminescent properties of these two metal-halide perovskite materials, we performed excitation-delay emission spectroscopy. The testing conditions involved collecting the excitation emission spectra 25 milliseconds after the excitation light was turned off. As shown in Figure S9, both 4-POMACC and 4-POEACC exhibit two luminescent centers, with their positions closely matching the phosphorescence emission observed in previous tests. Both materials display a single dominant excitation range, with 4-POMACC showing the strongest excitation from 260 nm to 290 nm, while 4-POEACC's peak excitation range is slightly different, focusing from 270 nm to 290 nm. Additionally, the luminescent centers of both materials do not shift with changes in excitation wavelength, indicating that the materials exhibit no excitation dependency and possess stable luminescent characteristics.

To gain a deeper understanding of the phosphorescence emission mechanism of 4-POMACC, we conducted a temperature test for both samples. Figure 8a shows the temperature-dependent phosphorescence spectra of 4-POMACC. It is evident that the phosphorescence intensity decreases as the temperature increases, which is attributed to the enhancement of molecular vibrations at high temperatures, leading to increased non-radiative transitions and reduced luminescence efficiency [43]. Figure 8b presents the CIE diagrams at different temperatures, illustrating that the color of the phosphorescence shifts with temperature changes, demonstrating a temperature-dependent color characteristic. Figure 8c plots the relationship between the emission peak position (peak 1, from organic molecules) and its full-width at half-maximum (FWHM) when temperature changes. As the temperature rises, the peak position exhibits a red shift, likely due to increased molecular vibrations at higher temperatures, leading to characteristics of aggregated luminescence [44]. The FWHM also increases, indicating enhanced coupling between phonons and electrons [45]. Figure 8d shows the temperature dependence of emission peak position (peak 2, from defect state) and its FWHM. With increasing temperature, the peak position shifts to the blue, possibly due to lattice expansion of the inorganic layers, which enlarges the bandgap. The FWHM also gradually increases, reflecting increased coupling between phonons and electrons. Similarly, the phosphorescence emission mechanism of 4-POEACC was also conducted as shown in Figure S10. It is evident that, as the temperature increases, the phosphorescence intensity gradually decreases, owing to the increased non-radiative transitions. Although 4-POEACC also shows a color dependence on temperature, the extent of color change with temperature is less pronounced compared to 4-POMACC. In addition, as temperature rises, the position of peak 1 remains unchanged, while the FWHM increases, indicating the enhanced coupling between phonons and electrons. The blue-shifted peak 2 with increasing temperature again confirms the lattice expansion of inorganic layers.

To fully understand the differences in luminescent performance between the two metal-halide perovskites, density functional theory (DFT) calculations were performed. Since the luminescence of both materials primarily originates from the organic molecules, we calculated the orbital distributions and intersystem crossing (ISC) rates for the organic

components of each material. Figure 9a,b present the orbital distribution diagrams for 4-POMA and 4-POEA, respectively. These diagrams reveal that the HOMO and LUMO energy levels of the two organic components have very similar band gaps, and the orbital distributions of both HOMO and LUMO are concentrated on the benzene rings. DFT calculations of the spin orbital coupling constants (ξ) for the S_1 and T_n (n = 1, 2, 3) states of the two organic components indicate that both 4-POMA and 4-POEA have excellent intersystem crossing. But, according to energy level diagrams of 4-POMA and 4-POEA (Figure 9c,d), the energy gap between T_3 and T_2 in 4-POMA is significantly greater than that of 4-POEA. Therefore, the internal conversion rate between T_3 and T_2 of 4-POMA is smaller than that of 4-POEA, which leads to a longer phosphorescence lifetime of 4-POME.

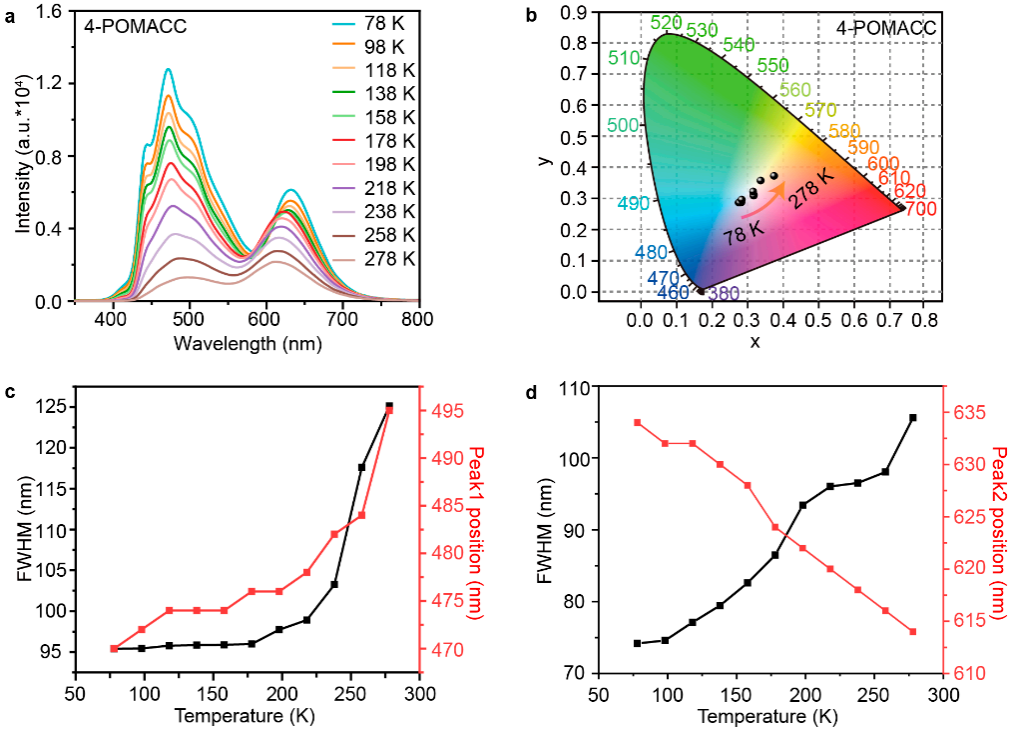


Figure 8. (**a**) Temperature-dependent emission spectra of 4-POMACC excited at 286 nm and (**b**) the corresponding CIE coordinate diagram. The intensity and FWHM variations in the two emission peaks from (**c**) organic molecule (peak 1) and (**d**) defect states (peak 2).

Encryption is a crucial technology in the information society nowadays [46–48]. Leveraging the distinct RTP properties of these two materials, we applied them in the field of information encryption. We coated molds marked with the number "9" with 4-POMACC and 4-POEACC materials. As illustrated in Figure 10, the area within the red dashed box is filled with 4-POEACC, and the area within the white dashed box is filled with 4-POMACC. Under UV light, the two materials exhibit different colors, so that the 4-POEACC region displays the UV light color, while the 4-POMACC region emits green light. At this point, the displayed information in the shape of a "9" appears to be false. Given the distinct RTP characteristics of these two materials, after 1 s of UV light being turned off, the pattern of the "9" will reveal only partial information (Figure 9). The area coated with 4-POMACC will continue to emit green light, revealing the true information. This approach effectively provides an encryption method based on the differing luminescent properties of the materials.

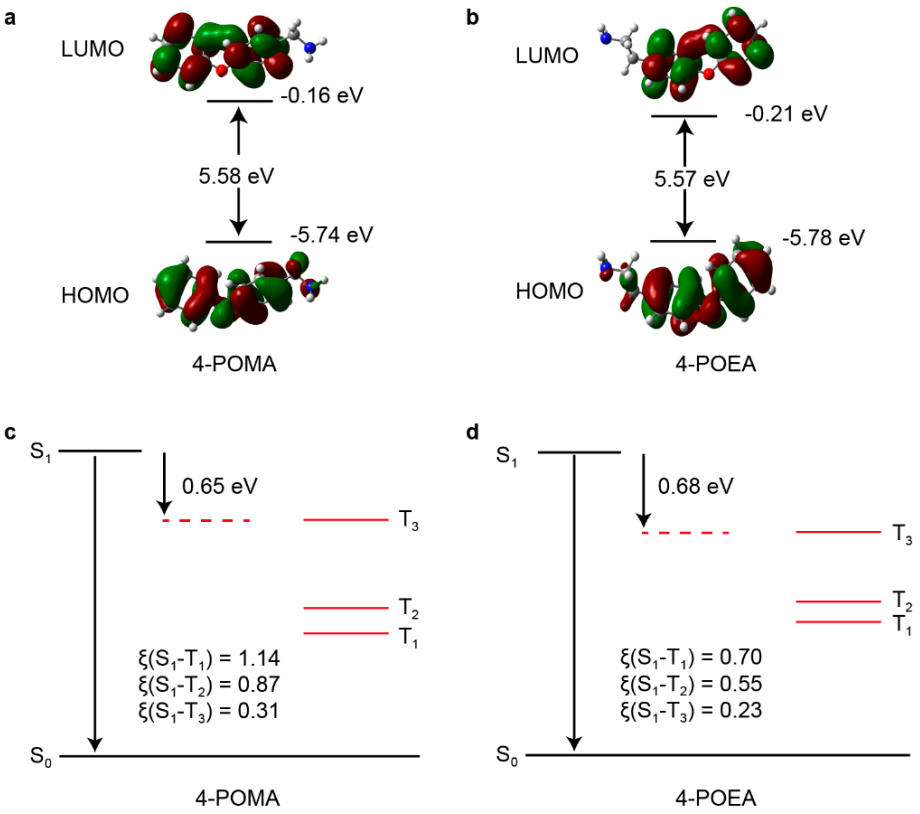


Figure 9. Orbital distribution diagrams for (**a**) 4-POMA and (**b**) 4-POEA. Energy level diagrams for (**c**) 4-POMA and (**d**) 4-POEA.

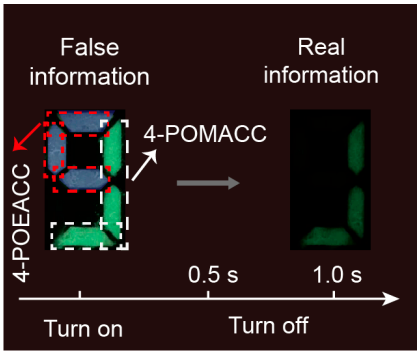


Figure 10. Demonstration of information encryption using 4-POMACC and 4-POEACC.

3. Materials and Methods

3.1. Materials

4-Phenoxybenzylamine (4-POMA, 98%), 4-phenoxyphenethylamine (4-POEA, 97%) and cadmium chloride ($CdCl_2$, 99%) were purchased from Aladdin (Shanghai, China) or Energy Chemical (Shanghai, China). HCl (37 wt.%, in water), ethanol and acetone were purchased from Nanjing Chemical Reagent Co., Ltd. (Nanjing, China). All reagents and solvents were used without further purifications.

3.2. Synthesis of Organic Amines Salts

Substance 4-POMACl. As shown in Figure S1, over an ice-water bath, 10 mL of ethanol was placed in a 50 mL round-bottom flask. To this system, 1.6 mmol (286 μL) of 4-POMA was added, followed by the dropwise addition of 4 mL of HCl with continuous stirring. As the solution was stirred, the product 4-POMACl began to precipitate out. After allowing the reaction to proceed for 1 h, the product was collected. The product was then subjected

to vacuum filtration using a filtration apparatus. During the filtration process, the products were washed six times with acetone. The washed products were stored in a centrifuge tube, sealed with parafilm, and placed in a vacuum drying oven for further characterization. The final yield product in this synthesis procedure was 0.3380 g (approximately 90%).

Substance 4-POEACl. The synthesis of 4-POEACl salts were carried out in a similar way to that of 4-POMACl by replacing 4-POMA with 4-POEA (1.6 mmol, 314 μL). The final yield product in this synthesis procedure was 0.2901 g (approximately 85%).

3.3. Synthesis of 2D Metal-Halide Perovskites

Substance 4-POMACC. As shown in Figure S2, under ambient conditions, 4-POMACl (0.8 mmol, 0.1886 g) and $CdCl_2$ (0.4 mmol, 0.0733 g) were placed in a 25 mL round-bottom flask. A measure of 5 mL of ethanol was added to this mixture, and the system was thoroughly shaken. The mixture was then heated to 85 °C and stirred continuously at this temperature for 1 h until a clear solution was obtained. The clear solution was then transferred to a clean sample vial. After allowing the vial to stand at room temperature for a period of time, the product 4-POMACC began to precipitate out. The product was then collected through vacuum filtration, washed 6 to 7 times with acetone, and stored in a centrifuge tube, sealed with parafilm. Finally, the product was placed in a vacuum drying oven for further characterizations. The final yield product in this synthesis procedure was 0.2279 g (approximately 87%).

Substance 4-POEACC. The synthesis of 4-POEACC was carried out in a similar way to that of 4-POMACC by replacing 4-POMAC with 4-POEAC (0.8 mmol, 0.1998 g), and the heating temperature was set to 80 °C. The final yield product was 0.2294 g (approximately 84%).

3.4. Characterization

Crystalline structures of the samples were measured by powder X-ray diffraction (PXRD) using a Bruker D8 Advance X diffractometer (Cu Kα: λ = 1.5418 Å, Bruker AXS GmbH, Karlsruhe, Germany). Thermogravimetric analyses (TGA) were conducted on a DTG-60 Shimadzu thermal analyst system (Shimadzu, Kyoto, Japan) with a heating rate of 10 °C/min and a nitrogen flow rate of 50 cm^3/min. Fourier transform infrared (FTIR) spectra were obtained on a Bruker VERTEX 70 (Bruker AXS GmbH, Karlsruhe, Germany). Scanning electron microscope (SEM) images were acquired using a Hitachi SU4800-II cFEG SEM (Hitachi, Tokyo, Japan) at an accelerating voltage of 2.0 kV. Ultraviolet/visible (UV/Vis) and fluorescence spectra were recorded on a Jasco V-750 spectrophotometer (Jasco, Tokyo, Japan) and Edinburgh FLS980 (EI, Edinburgh, Germany), respectively. The absolute photoluminescence quantum yield (PLQY) was obtained using an Edinburgh FLS980 fluorescence spectrophotometer equipped with an integrating sphere. For fluorescence decay measurements, picosecond pulsed light-emitting diode (EPLED-380, Yida, Shenzhen, China, wavelength: 377 nm, pulse width: 947.7 ps; EPLED-295, Yida, Shenzhen, China, wavelength: 300 nm, pulse width: 833.7 ps) were used. Phosphorescence spectra were obtained using an Edinburgh FLS980 fluorescence spectrophotometer with a 10 ms delay time after excitation using a microsecond flash lamp. The microsecond flash lamp produces short, typically a few μs, and high irradiance optical pulses for phosphorescence decay measurements ranging from microseconds to seconds. The kinetic measurements, afterglow spectra and lifetimes were measured using an Edinburgh FLS980 fluorescence spectrophotometer and a microsecond flash-lamp (μF900). The lifetime and time-resolved emission spectra were obtained on Edinburgh FLSP 920 fluorescence spectrophotometer (EI, Edinburgh, Germany) equipped with a xenon arc lamp (Xe 900), a nanosecond hydrogen flash-lamp (nF 920), or a microsecond flash-lamp (μF900). The lifetimes (τ) of the luminescence were obtained by fitting the decay curve with a multi-exponential decay function.

Excitation–phosphorescence mapping was measured using Hitachi F-4700 (Hitachi, Tokyo, Japan) with a 25 ms delay time under ambient conditions.

3.5. Computational Methods

DFT calculations were performed to investigate the singlet-to-triplet exciton transformation using the Gaussian 09 package. The ground-state structures were optimized at the B3LYP/6-31G(d) level of theory. The first triplet excited state (T_1) was subsequently optimized at the same level based on the optimized ground-state geometry. Using time-dependent DFT (TD-DFT), the vertical excitation energies of the designed materials were calculated at the B3LYP/6-31G(d) level. Based on the optimized T_1 geometric structure, the spin-orbit coupling (SOC) between the S_1 state and the T_1, T_2, and T_3 states of the two materials was computed using the Dalton 2020 software package at the B3LYP/6-31G* level of theory. The Hirshfeld surfaces and 2D fingerprint plots were calculated by using Crystal Explorer 17. And d_i is the distance between the Hirshfeld surface and the nearest atom inside the Hirshfeld surface, while de is the distance between the Hirshfeld surface and the nearest atom outside the Hirshfeld surface. The intense of the color in the fingerprint plots represents the contribution of a pair (d_i, d_e) on the Hirshfeld surface.

4. Conclusions

In this work, two organic amines with different alkyl chain lengths were selected as organic components and $CdCl_2$ was selected as the inorganic framework due to its heavy-atom effect, which can enhance the intersystem crossing rate and strengthen triplet-state luminescence to synthesize 2D metal-halide perovskites 4-POMACC and 4-POEACC. Layer-spacing calculations suggest that 4-POMACC is more densely packed compared to 4-POEACC, which is favorable for RTP emission. Comprehensive studies of the optical properties confirm that these two materials exhibit significant differences in their RTP characteristics. Specifically, 4-POMACC has a much longer RTP lifetime than 4-POEACC. DFT calculations reveal a greater likelihood of intersystem crossing in 4-POMA and thus more effective triplet-state emission. Based on the RTP properties of these 2D metal-halide perovskites, the materials were applied in anti-counterfeiting applications. This study provides a new approach for regulating RTP in 2D metal-halide perovskites and enriches the variety of RTP materials.

Supplementary Materials: The following supporting information can be downloaded at: https://www.mdpi.com/article/10.3390/inorganics13040108/s1, Figure S1: The synthesis process of preparing organic amines salts in this work; Figure S2: The synthesis process of preparing 2D metal-halide perovskites in this work; Figure S3: Fourier transform infrared patterns of (a) 4-POMACC and (b) 4-POEACC, as well as their corresponding organic amine salts (4-POMACl and 4-POEACl); Figure S4: Thermogravimetry and derivative thermogravimetry curves of (a) 4-POMACC, (b) 4-POEACC, (c) 4-POMACl, and (d) 4-PAEACl; Figure S5: Time-resolved emission spectroscopy results of (a) 4-POMACC and (b) 4-POEACC; Figure S6: Photoluminescence quantum efficiency measurement results of (a) 4-POMACl, (b) 4-POMACC, (c) 4-POEACl, and (d) 4-POEACC; Figure S7: Double-exponential linear fitting of excitation power vs. phosphorescence intensity for (a) 4-POMACC and (b) 4-POEACC; Figure S8: (a) Fluorescence and (b) phosphorescence intensities of 4-POMACC and 4-POEACC at differing radiation flux. (c) Fluorescence and (d) phosphorescence intensities of 4-POMACC and 4-POEACC under different excitation duration; Figure S9: Time-resolved phosphorescence emission spectroscopy of (a) 4-POMACC and (b) 4-POEACC; Figure S10: (a) Temperature-dependent emission spectra of 4-POEACC excited at 284 nm and (b) the corresponding CIE coordinate diagram. The intensity and FWHM variations of two emission peaks from (c) organic molecule (peak 1) and (d) defect states (peak 2).

Author Contributions: Conceptualization, Z.L. and G.Z.; methodology, H.Z.; software, S.W., B.S. and Y.H.; validation, Z.L., B.S. and Y.H.; formal analysis, M.S. and M.L.; investigation, G.Z.; resources, G.Z.; data curation, H.Z.; writing—original draft preparation, H.Z. and S.W.; writing—review and editing, B.S. and Y.H.; visualization, S.W., M.S. and M.L.; supervision, Z.L. and G.Z.; project administration, B.S., Y.H. and G.Z.; funding acquisition, Z.L. and G.Z. All authors have read and agreed to the published version of the manuscript.

Funding: This research was funded by Shandong Provincial Natural Science Foundation, grant number ZR2024QF165.

Institutional Review Board Statement: Not applicable.

Informed Consent Statement: Not applicable.

Data Availability Statement: The original contributions presented in the study are included in the article/Supplementary Materials; further inquiries can be directed to the corresponding authors.

Acknowledgments: We thank Zhiyan Zhou from School of Stomatology, Shandong University, for her help with language polishing.

Conflicts of Interest: The authors declare no conflicts of interest.

References

1. Wang, B.; Mu, Y.; Zhang, H.; Shi, H.; Chen, G.; Yu, Y.; Yang, Z.; Li, J.; Yu, J. Red Room-Temperature Phosphorescence of CDs@Zeolite Composites Triggered by Heteroatoms in Zeolite Frameworks. *ACS Cent. Sci.* **2019**, *5*, 349–356. [CrossRef] [PubMed]
2. Ma, X.-K.; Liu, Y. Supramolecular Purely Organic Room-Temperature Phosphorescence. *Acc. Chem. Res.* **2021**, *54*, 3403–3414. [CrossRef]
3. Zhi, J.; Zhou, Q.; Shi, H.; An, Z.; Huang, W. Organic Room Temperature Phosphorescence Materials for Biomedical Applications. *Chem.—Asian J.* **2020**, *15*, 947–957. [CrossRef]
4. Yang, J.; Zhen, X.; Wang, B.; Gao, X.; Ren, Z.; Wang, J.; Xie, Y.; Li, J.; Peng, Q.; Pu, K.; et al. The Influence of the Molecular Packing on the Room Temperature Phosphorescence of Purely Organic Luminogens. *Nat. Commun.* **2018**, *9*, 840. [CrossRef] [PubMed]
5. Peng, Q.; Ma, H.; Shuai, Z. Theory of Long-Lived Room-Temperature Phosphorescence in Organic Aggregates. *Acc. Chem. Res.* **2021**, *54*, 940–949. [CrossRef]
6. Manser, J.S.; Saidaminov, M.I.; Christians, J.A.; Bakr, O.M.; Kamat, P.V. Making and Breaking of Lead Halide Perovskites. *Acc. Chem. Res.* **2016**, *49*, 330–338. [CrossRef]
7. Zhang, W.; Eperon, G.E.; Snaith, H.J. Metal Halide Perovskites for Energy Applications. *Nat. Energy* **2016**, *1*, 16048. [CrossRef]
8. Jena, A.K.; Kulkarni, A.; Miyasaka, T. Halide Perovskite Photovoltaics: Background, Status, and Future Prospects. *Chem. Rev.* **2019**, *119*, 3036–3103. [CrossRef] [PubMed]
9. Stranks, S.D.; Snaith, H.J. Metal-Halide Perovskites for Photovoltaic and Light-Emitting Devices. *Nat. Nanotechnol.* **2015**, *10*, 391–402. [CrossRef]
10. Stoumpos, C.C.; Kanatzidis, M.G. The Renaissance of Halide Perovskites and Their Evolution as Emerging Semiconductors. *Acc. Chem. Res.* **2015**, *48*, 2791–2802. [CrossRef]
11. Ortiz-Cervantes, C.; Carmona-Monroy, P.; Solis-Ibarra, D. Two-Dimensional Halide Perovskites in Solar Cells: 2D or Not 2D? *ChemSusChem* **2019**, *12*, 1560–1575. [CrossRef]
12. Ghimire, S.; Klinke, C. Two-Dimensional Halide Perovskites: Synthesis, Optoelectronic Properties, Stability, and Applications. *Nanoscale* **2021**, *13*, 12394–12422. [CrossRef]
13. Shi, E.; Gao, Y.; Finkenauer, B.P.; Akriti, A.; Coffey, A.H.; Dou, L. Two-Dimensional Halide Perovskite Nanomaterials and Heterostructures. *Chem. Soc. Rev.* **2018**, *47*, 6046–6072. [CrossRef] [PubMed]
14. Liu, Y.; Xiao, H.; Goddard, W.A. Two-Dimensional Halide Perovskites: Tuning Electronic Activities of Defects. *Nano Lett.* **2016**, *16*, 3335–3340. [CrossRef] [PubMed]
15. Mao, L.; Stoumpos, C.C.; Kanatzidis, M.G. Two-Dimensional Hybrid Halide Perovskites: Principles and Promises. *J. Am. Chem. Soc.* **2019**, *141*, 1171–1190. [CrossRef] [PubMed]
16. Huo, C.; Cai, B.; Yuan, Z.; Ma, B.; Zeng, H. Two-Dimensional Metal Halide Perovskites: Theory, Synthesis, and Optoelectronics. *Small Methods* **2017**, *1*, 1600018. [CrossRef]
17. Ba, Q.; Jana, A.; Wang, L.; Kim, K.S. Dual Emission of Water-Stable 2D Organic–Inorganic Halide Perovskites with Mn(II) Dopant. *Adv. Funct. Mater.* **2019**, *29*, 1904768. [CrossRef]

18. Quan, L.N.; Zhao, Y.; García De Arquer, F.P.; Sabatini, R.; Walters, G.; Voznyy, O.; Comin, R.; Li, Y.; Fan, J.Z.; Tan, H.; et al. Tailoring the Energy Landscape in Quasi-2D Halide Perovskites Enables Efficient Green-Light Emission. *Nano Lett.* **2017**, *17*, 3701–3709. [CrossRef]
19. Yu, J.; Kong, J.; Hao, W.; Guo, X.; He, H.; Leow, W.R.; Liu, Z.; Cai, P.; Qian, G.; Li, S.; et al. Broadband Extrinsic Self-Trapped Exciton Emission in Sn-Doped 2D Lead-Halide Perovskites. *Adv. Mater.* **2019**, *31*, 1806385. [CrossRef]
20. Smith, M.D.; Karunadasa, H.I. White-Light Emission from Layered Halide Perovskites. *Acc. Chem. Res.* **2018**, *51*, 619–627. [CrossRef]
21. Nawab, G.; Rahman, A.U.; Haq, I.U.; Ali, A.; Abdelkader, A.; Ismail, A.H.; Alomar, M.; Khan, I. Structural and Optoelectronic Properties of 2D Halide Perovskites Cs2MBr4 (M = Zn, Cd, Hg): A First Principle Study. *Opt. Quantum Electron.* **2024**, *56*, 871. [CrossRef]
22. Yangui, A.; Pillet, S.; Bendeif, E.-E.; Lusson, A.; Triki, S.; Abid, Y.; Boukheddaden, K. Broadband Emission in a New Two-Dimensional Cd-Based Hybrid Perovskite. *ACS Photonics* **2018**, *5*, 1599–1611. [CrossRef]
23. Cai, T.; Yang, H.; Hills-Kimball, K.; Song, J.-P.; Zhu, H.; Hofman, E.; Zheng, W.; Rubenstein, B.M.; Chen, O. Synthesis of All-Inorganic Cd-Doped $CsPbCl_3$ Perovskite Nanocrystals with Dual-Wavelength Emission. *J. Phys. Chem. Lett.* **2018**, *9*, 7079–7084. [CrossRef]
24. Holder, C.F.; Fanghanel, J.; Xiong, Y.; Dabo, I.; Schaak, R.E. Phase-Selective Solution Synthesis of Perovskite-Related Cesium Cadmium Chloride Nanoparticles. *Inorg. Chem.* **2020**, *59*, 11688–11694. [CrossRef] [PubMed]
25. Hoffman, J.M.; Malliakas, C.D.; Sidhik, S.; Hadar, I.; McClain, R.; Mohite, A.D.; Kanatzidis, M.G. Long Periodic Ripple in a 2D Hybrid Halide Perovskite Structure Using Branched Organic Spacers. *Chem. Sci.* **2020**, *11*, 12139–12148. [CrossRef]
26. Zhou, N.; Zhou, H. Spacer Organic Cation Engineering for Quasi-2D Metal Halide Perovskites and the Optoelectronic Application. *Small Struct.* **2022**, *3*, 2100232. [CrossRef]
27. Li, X.; Hoffman, J.M.; Kanatzidis, M.G. The 2D Halide Perovskite Rulebook: How the Spacer Influences Everything from the Structure to Optoelectronic Device Efficiency. *Chem. Rev.* **2021**, *121*, 2230–2291. [CrossRef]
28. Gan, L.; Li, J.; Fang, Z.; He, H.; Ye, Z. Effects of Organic Cation Length on Exciton Recombination in Two-Dimensional Layered Lead Iodide Hybrid Perovskite Crystals. *J. Phys. Chem. Lett.* **2017**, *8*, 5177–5183. [CrossRef]
29. Deng, C.; Zhou, G.; Chen, D.; Zhao, J.; Wang, Y.; Liu, Q. Broadband Photoluminescence in 2D Organic–Inorganic Hybrid Perovskites: $(C_7H_{18}N_2)PbBr_4$ and $(C_9H_{22}N_2)PbBr_4$. *J. Phys. Chem. Lett.* **2020**, *11*, 2934–2940. [CrossRef]
30. Kamminga, M.E.; Fang, H.-H.; Filip, M.R.; Giustino, F.; Baas, J.; Blake, G.R.; Loi, M.A.; Palstra, T.T.M. Confinement Effects in Low-Dimensional Lead Iodide Perovskite Hybrids. *Chem. Mater.* **2016**, *28*, 4554–4562. [CrossRef]
31. Smith, M.D.; Connor, B.A.; Karunadasa, H.I. Tuning the Luminescence of Layered Halide Perovskites. *Chem. Rev.* **2019**, *119*, 3104–3139. [CrossRef]
32. Gong, J.; Hao, M.; Zhang, Y.; Liu, M.; Zhou, Y. Layered 2D Halide Perovskites beyond the Ruddlesden–Popper Phase: Tailored Interlayer Chemistries for High-Performance Solar Cells. *Angew. Chem.* **2022**, *134*, e202112022. [CrossRef]
33. Gao, S.; Wang, S.; Wu, J.; Lin, Z. Regulation and Application of Organic Luminescence from Low-Dimensional Organic–Inorganic Hybrid Metal Halides. *J. Mater. Chem. C* **2023**, *11*, 16890–16911. [CrossRef]
34. Dhanabalan, B.; Castelli, A.; Palei, M.; Spirito, D.; Manna, L.; Krahne, R.; Arciniegas, M. Simple Fabrication of Layered Halide Perovskite Platelets and Enhanced Photoluminescence from Mechanically Exfoliated Flakes. *Nanoscale* **2019**, *11*, 8334–8342. [CrossRef] [PubMed]
35. Liu, Z.; Qin, X.; Chen, Q.; Jiang, T.; Chen, Q.; Liu, X. Metal–Halide Perovskite Nanocrystal Superlattice: Self-Assembly and Optical Fingerprints. *Adv. Mater.* **2023**, *35*, 2209279. [CrossRef]
36. Bright, D.W.; Dias, F.B.; Galbrecht, F.; Scherf, U.; Monkman, A.P. The Influence of Alkyl-Chain Length on Beta-Phase Formation in Polyfluorenes. *Adv. Funct. Mater.* **2009**, *19*, 67–73. [CrossRef]
37. Crosby, G.A.; Demas, J.N. Measurement of Photoluminescence Quantum Yields. Review. *J. Phys. Chem.* **1971**, *75*, 991–1024. [CrossRef]
38. Duan, X.; Song, W.; Qiao, J.; Li, X.; Cai, Y.; Wu, H.; Zhang, J.; Hao, X.; Tang, Z.; Ge, Z.; et al. Ternary Strategy Enabling High-Efficiency Rigid and Flexible Organic Solar Cells with Reduced Non-Radiative Voltage Loss. *Energy Environ. Sci.* **2022**, *15*, 1563–1572. [CrossRef]
39. Liu, Z.; Qin, X.; Chen, Q.; Chen, Q.; Jing, Y.; Zhou, Z.; Zhao, Y.S.; Chen, J.; Liu, X. Highly Stable Lead-Free Perovskite Single Crystals with NIR Emission Beyond 1100 Nm. *Adv. Opt. Mater.* **2022**, *10*, 2201254. [CrossRef]
40. Peng, Y.; Ma, J.; Zhao, Y.; You, D.; Yao, Y.; Deng, Z.; Liao, J.; Chang, Y.; Shen, W.; Li, M.; et al. Multilevel Stimulus-Responsive Room Temperature Phosphorescence Achieved by Efficient Energy Transfer from Triplet Excitons to Mn^{2+} Pairs in 2D Hybrid Metal Halide. *Adv. Funct. Mater.* **2024**, 2420311. [CrossRef]
41. Luo, B.; Liang, D.; Sun, S.; Xiao, Y.; Lian, X.; Li, X.; Li, M.-D.; Huang, X.-C.; Zhang, J.Z. Breaking Forbidden Transitions for Emission of Self-Trapped Excitons in Two Dimensional $(F_2CHCH_2NH_3)_2CdBr_4$ Perovskite through Pb Alloying. *J. Phys. Chem. Lett.* **2020**, *11*, 199–205. [CrossRef] [PubMed]

42. Goushi, K.; Yamada, T.; Otomo, A. Excitation Intensity Dependence of Power-Law Blinking Statistics in Nanocrystal Quantum Dots. *J. Phys. Chem. C* **2009**, *113*, 20161–20168. [CrossRef]
43. Kim, Y.H.; Arunkumar, P.; Kim, B.Y.; Unithrattil, S.; Kim, E.; Moon, S.-H.; Hyun, J.Y.; Kim, K.H.; Lee, D.; Lee, J.-S.; et al. A Zero-Thermal-Quenching Phosphor. *Nat. Mater.* **2017**, *16*, 543–550. [CrossRef]
44. Yang, J.; Fang, M.; Li, Z. Organic Luminescent Materials: The Concentration on Aggregates from Aggregation-induced Emission. *Aggregate* **2020**, *1*, 6–18. [CrossRef]
45. Gong, Z.; Li, Z.; Zhong, Y. Circularly Polarized Luminescence of Coordination Aggregates. *Aggregate* **2022**, *3*, e177. [CrossRef]
46. Su, Y.; Phua, S.Z.F.; Li, Y.; Zhou, X.; Jana, D.; Liu, G.; Lim, W.Q.; Ong, W.K.; Yang, C.; Zhao, Y. Ultralong Room Temperature Phosphorescence from Amorphous Organic Materials toward Confidential Information Encryption and Decryption. *Sci. Adv.* **2018**, *4*, eaas9732. [CrossRef]
47. Liu, S.; Liu, X.; Yuan, J.; Bao, J. Multidimensional Information Encryption and Storage: When the Input Is Light. *Research* **2021**, *2021*, 7897849. [CrossRef]
48. Tan, J.; Li, Q.; Meng, S.; Li, Y.; Yang, J.; Ye, Y.; Tang, Z.; Qu, S.; Ren, X. Time-Dependent Phosphorescence Colors from Carbon Dots for Advanced Dynamic Information Encryption. *Adv. Mater.* **2021**, *33*, 2006781. [CrossRef]

Disclaimer/Publisher's Note: The statements, opinions and data contained in all publications are solely those of the individual author(s) and contributor(s) and not of MDPI and/or the editor(s). MDPI and/or the editor(s) disclaim responsibility for any injury to people or property resulting from any ideas, methods, instructions or products referred to in the content.